

# Hierarchical Nanomorphologies Promote Exciton Dissociation in Polymer/Fullerene Bulk Heterojunction Solar Cells

Wei Chen,<sup>\*,†</sup> Tao Xu,<sup>‡</sup> Feng He,<sup>‡</sup> Wei Wang,<sup>‡</sup> Cheng Wang,<sup>§</sup> Joseph Strzalka,<sup>||</sup> Yun Liu,<sup>⊥,¶</sup> Jianguo Wen,<sup>□</sup> Dean J. Miller,<sup>□</sup> Jihua Chen,<sup>○</sup> Kunlun Hong,<sup>○</sup> Luping Yu,<sup>\*,‡</sup> and Seth B. Darling<sup>\*,†</sup>

<sup>†</sup>Center for Nanoscale Materials, Argonne National Laboratory, 9700 South Cass Avenue, Lemont, Illinois 60439, United States

<sup>‡</sup>Department of Chemistry and The James Franck Institute, The University of Chicago, 929 East 57th Street, Chicago, Illinois 60637, United States

<sup>§</sup>Advanced Light Source, Lawrence Berkeley National Laboratory, Berkeley, California 94720, United States

<sup>||</sup>X-ray Science Division, Advanced Photon Source, Argonne National Laboratory, Lemont, Illinois 60439, United States

<sup>⊥</sup>NIST Center for Neutron Research, National Institute of Standards and Technology, Gaithersburg, Maryland 20899, United States

<sup>¶</sup>Department of Chemical Engineering, University of Delaware, Newark, Delaware 19716, United States

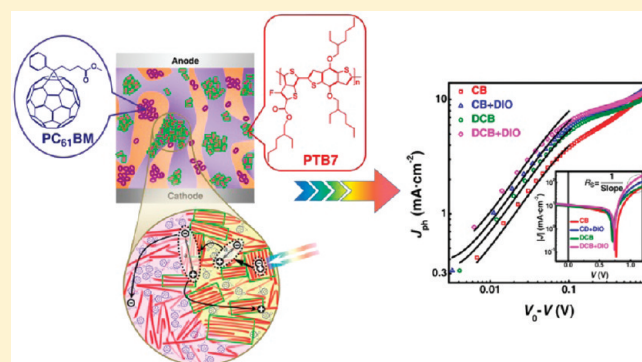
<sup>□</sup>Electron Microscopy Center and Materials Science Division, Argonne National Laboratory, Lemont, Illinois 60439, United States

<sup>○</sup>Center for Nanophase Materials Sciences, Oak Ridge National Laboratory, Oak Ridge, Tennessee 37831, United States

**S** Supporting Information

**ABSTRACT:** PTB7 semiconducting copolymer comprising thieno[3,4-b]thiophene and benzodithiophene alternating repeat units set a historic record of solar energy conversion efficiency (7.4%) in polymer/fullerene bulk heterojunction solar cells. To further improve solar cell performance, a thorough understanding of structure–property relationships associated with PTB7/fullerene and related organic photovoltaic (OPV) devices is crucial. Traditionally, OPV active layers are viewed as an interpenetrating network of pure polymers and fullerenes with discrete interfaces. Here we show that the active layer of PTB7/fullerene OPV devices in fact involves hierarchical nanomorphologies ranging from several nanometers of crystallites to tens of nanometers of nanocrystallite aggregates in PTB7-rich and fullerene-rich domains, themselves hundreds of nanometers in size. These hierarchical nanomorphologies are coupled to significantly enhanced exciton dissociation, which consequently contribute to photocurrent, indicating that the nanostructural characteristics at multiple length scales is one of the key factors determining the performance of PTB7 copolymer, and likely most polymer/fullerene systems, in OPV devices.

**KEYWORDS:** Organic photovoltaics, bulk heterojunction, hierarchical nanomorphology, charge photogeneration, X-ray scattering, device performance



Solar cells based on the polymer/fullerene bulk heterojunction (BHJ) represent one of the most promising technologies for next-generation solar energy conversion due to their low-cost and scalability.<sup>1–3</sup> In the last fifteen years, research efforts have led to organic photovoltaic (OPV) devices with power conversion efficiencies (PCEs) up to 7–8%,<sup>4–9</sup> but these values are still insufficient for the devices to become widely marketable. A growing number of studies have pointed out that the morphology of the active layer is of major importance in polymer/fullerene BHJ solar cells.<sup>10–12</sup> Still, further improvement is impeded by poor understanding of the correlations between structure and performance. The current BHJ paradigm pictures an ideal morphology involving a bicontinuous interpenetrating network of pure donor and acceptor domains, which should exhibit a maximal area of discrete interfaces for efficient exciton dissociation and a phase-separated dimension

commensurate with the exciton diffusion length but greater than the Coulomb capture radius for effective charge transport.<sup>2,3,12–14</sup> This morphology, however, requires a trade-off between exciton dissociation and charge transport to minimize charge recombination and thus maximize charge photogeneration. In fact, recent studies of phase purity,<sup>15–19</sup> interface morphology,<sup>20–23</sup> and ordering of materials at different length scales<sup>23–26</sup> have challenged this ideal BHJ model. Thus, it is necessary to more fully decipher the complex structure–property relationships in the OPV devices, and consequently, to refine the current BHJ model.

**Received:** May 20, 2011

**Revised:** July 19, 2011

**Published:** August 08, 2011

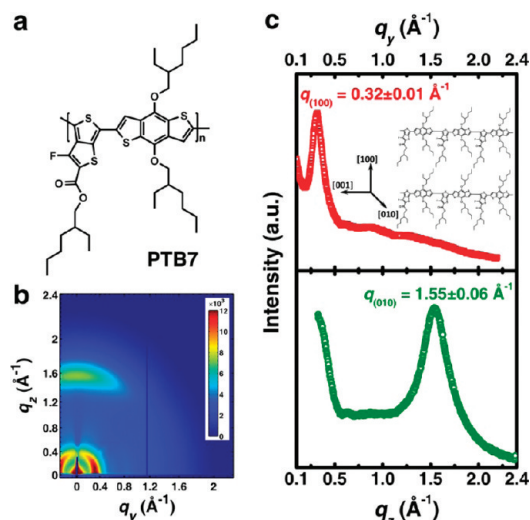


**Figure 1.** (a) The chemical structure of the PTB7 copolymer. (b) The 2D GIWAXS pattern and (c) the corresponding  $q_y$  and  $q_z$  scans of a thin film of neat PTB7 homopolymer on a bare Si substrate. The inset delineates a schematic of crystallographic directions of the PTB7 copolymer chains. The PTB7 layers lie in the (100) plane, the [100] direction is normal to the PTB7 layers, the  $\pi$ -face lies in the (010) plane, the  $\pi$ - $\pi$  stacking direction is along the [010] direction, and the chain backbone is along the [001] direction.

In this work, we used PTB7 semiconducting copolymer ( $M_n = 42\,000$  and  $PDI = 2.2$ ) that contains thieno[3,4-*b*]thiophene and benzodithiophene alternating units<sup>4–6</sup> (Figure 1a) as an archetype of high-performance polymer/fullerene BHJ solar cells, given that PTB7 has set a historic record of PCE (7.4%) in BHJ solar cells when combined with fullerenes, very close to a commercially viable PCE of 10%.<sup>27</sup> We probed performance-related structures at different length scales, in particular, molecular organization and phase-separated morphology by several scattering techniques. Using a simple yet effective route, altering solvents,<sup>28–34</sup> to tune both crystalline structure and phase-separated morphology, and thereby, to improve performance, we elucidate a fundamental mechanistic connection between morphology and device performance; the superior performance of PTB7/fullerene BHJ solar cells is attributed to hierarchical nanomorphologies with optimum crystallinity and intermixing of PTB7 with PC<sub>61</sub>BM, which together promote exciton dissociation, and consequently, contribute to photocurrent.

We performed grazing incidence wide-angle X-ray scattering (GIWAXS) to acquire structural information, such as molecular orientation, intermolecular distances and crystallite sizes. Shown in Figure 1b,c are the 2D GIWAXS pattern and its in-plane ( $q_y$ ) and out-of-plane ( $q_z$ ) scans of a thin film of neat PTB7 homopolymer on a bare Si substrate, respectively. A distinct in-plane peak at  $q_y = 0.32 \pm 0.01 \text{ \AA}^{-1}$ , arising from the (100) Bragg diffraction, corresponds to periodic PTB7 lamellae with spacing of  $19.8 \pm 0.8 \text{ \AA}$ , comparable to the cross-sectional diameter of a single PTB7 copolymer chain when dissolved in a good solvent where the side chains are fully extended (small angle neutron scattering (SANS) data in Supporting Information Figure S1). The other out-of-plane peak from the (010) Bragg diffraction at  $q_z = 1.55 \pm 0.06 \text{ \AA}^{-1}$ , which is associated with  $\pi$ - $\pi$  stacking spacing of  $4.0 \pm 0.2 \text{ \AA}$ , suggests that the  $\pi$ - $\pi$  stacking is perpendicular to the substrate, that is, the  $\pi$ -faces are approximately parallel to the substrate. This is in agreement with previous reports of face-on conformation in the PTB series of copolymers.<sup>35,36</sup>

For comparison, 2D GIWAXS patterns of four thin films of PTB7 and [6,6]-phenyl C61 butyric acid methyl ester (PC<sub>61</sub>BM) blends and their  $q_y$  and  $q_z$  scans are shown in Figure 2a–f. It should be noted that all four films have a similar film thickness of  $\sim 80 \text{ nm}$  and were spin-cast on poly(3,4-ethylenedioxythiophene)/poly(styrenesulfonate) (PEDOT/PSS)-modified Si substrates using the following four different solvents: pure chlorobenzene (CB), mixtures of CB and 1,8-diiodooctane (DIO) (98:2 v/v%) (CB+DIO), pure 1,2-dichlorobenzene (DCB), and mixtures of DCB and DIO (98:2 v/v%) (DCB+DIO). For simplicity, the corresponding thin films are designated as PTB7/PC<sub>61</sub>BM/CB, PTB7/PC<sub>61</sub>BM/CB+DIO, PTB7/PC<sub>61</sub>BM/DCB, and PTB7/PC<sub>61</sub>BM/DCB+DIO in the following text. In GIWAXS patterns of the four films (Figure 2a–d), the (100) scattering of PTB7 copolymer exhibits similar ring-like patterns at  $q = 0.3 - 0.4 \text{ \AA}^{-1}$  and the (010) scattering is only observed out of plane, suggesting that PTB7 copolymer chains mainly remain in the face-on conformation, though with a more random orientation. On the other hand, the corresponding  $q_y$  scans reveal shifts of the (100) peaks from  $q_y = 0.32 \pm 0.01 \text{ \AA}^{-1}$  for neat PTB7 homopolymer to a larger  $q$  value of  $0.33 \pm 0.01 \text{ \AA}^{-1}$  for PTB7/PC<sub>61</sub>BM/CB and PTB7/PC<sub>61</sub>BM/CB+DIO,  $0.37 \pm 0.01 \text{ \AA}^{-1}$  for PTB7/PC<sub>61</sub>BM/DCB, and  $0.35 \pm 0.01 \text{ \AA}^{-1}$  for PTB7/PC<sub>61</sub>BM/DCB+DIO (Figure 2e). These shifts indicate the extent of interdigitation between alkyl side chains in PTB7/PC<sub>61</sub>BM blends, evident in different degrees of decrease in the interstack spacing of PTB7 lamellae from  $19.8 \pm 0.8 \text{ \AA}$  to  $17.1 \pm 0.7 \text{ \AA}$ . Furthermore, the scattering along  $q_z$  exhibits two peaks that partially overlap (Figure 2f). These two peaks were resolved by two Gaussian functions centered at  $q_z = 1.35 \pm 0.05 \text{ \AA}^{-1}$  and  $q_z = 1.70 \pm 0.06 \text{ \AA}^{-1}$ , corresponding to the (311) Bragg diffraction of C<sub>60</sub><sup>36–38</sup> and a  $\pi$ - $\pi$  stacking spacing of  $3.7 \pm 0.2 \text{ \AA}$  between PTB7 chains, respectively. The full widths at half-maximum (fwhm) of scattering peaks correlate to nanocrystallite sizes via the Scherrer equation,<sup>35,36</sup>  $D_L = 2(\ln 2/\pi)^{1/2} 2\pi(\Delta q)^{-1}$ , where  $\Delta q$  is the intrinsic fwhm of the peak given by  $\Delta q = [(\Delta q)_{\text{experiment}}^2 - (\Delta q)_{\text{resolution}}^2]^{1/2}$ .<sup>39,40</sup> Regardless of the solvents used, the crystallite sizes of PTB7 (100) lamellae are estimated to be  $\sim 3\text{--}4 \text{ nm}$ , which corresponds to roughly two or three stacked PTB7 lamellae, and those of both PTB7 (010)  $\pi$ - $\pi$  stacks and PC<sub>61</sub>BM is  $\sim 2 \text{ nm}$ , which approximates to six  $\pi$ -stacked copolymer chains and three units of C<sub>60</sub> ( $\sim 7 \text{ \AA}$ ), respectively. Taken together, the GIWAXS results indicate that the solvent selection neither significantly changes the organization of PTB7 copolymer chains at a molecular level nor the nanocrystallite sizes of PTB7 or PC<sub>61</sub>BM, beyond interdigitation of alkyl side chains.

Next, we evaluate crystallinity throughout the four PTB7/PC<sub>61</sub>BM films using high-resolution X-ray reflectivity (XRR). As the critical angle for total external reflection,<sup>41</sup>  $\theta_c$  is only proportional to the mass density  $\rho$  of PTB7/PC<sub>61</sub>BM blends with the same composition, the change in  $\theta_c$  directly reflects variations in crystallinity in the thin films. Figure 2g depicts XRR profiles of the four PTB7/PC<sub>61</sub>BM thin films. The two vertical dotted lines indicate the critical angles of PTB7/PC<sub>61</sub>BM at  $\sim 0.18^\circ$  and the Si substrate at  $\sim 0.24^\circ$ , respectively. Clearly, the critical angles of the four PTB7/PC<sub>61</sub>BM thin films are different from each other while the critical angle of the Si substrate remains constant, indicating solvent selection affects crystallinity in the PTB7/PC<sub>61</sub>BM films. Comparing the experimental data with the calculated XRR profiles, the  $\theta_c$ 's of PTB7/PC<sub>61</sub>BM thin films are quantitatively obtained as  $0.180^\circ$  for PTB7/PC<sub>61</sub>BM/CB,  $0.182^\circ$  for PTB7/PC<sub>61</sub>BM/CB+DIO,  $0.186^\circ$  for PTB7/PC<sub>61</sub>BM/DCB, and  $0.188^\circ$  for PTB7/PC<sub>61</sub>BM/DCB+DIO, indicating that the use of DCB and DIO additives, in contrast to pure CB, improves crystallinity, similar to observations in other



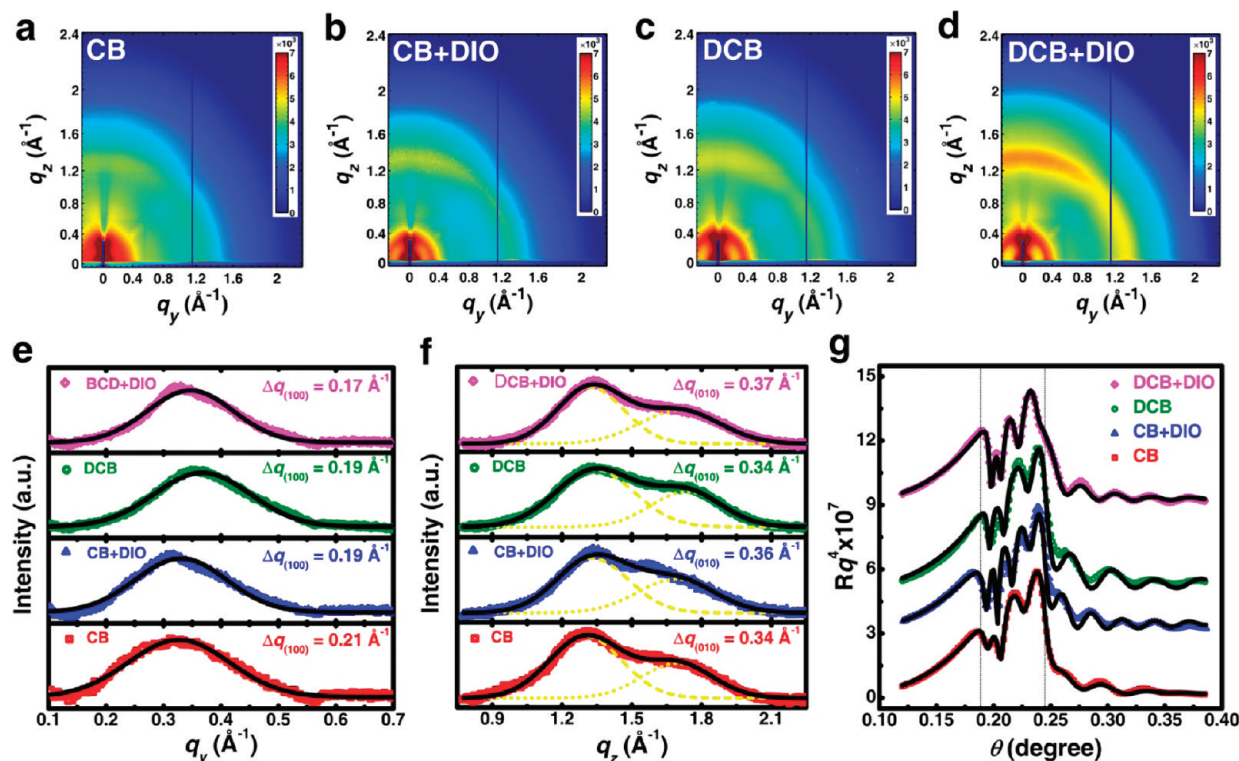


**Figure 2.** (a–d) The 2D GIWAXS patterns of the thin films of PTB7/PC<sub>61</sub>BM/CB, PTB7/PC<sub>61</sub>BM/CB+DIO, PTB7/PC<sub>61</sub>BM/DCB, and PTB7/PC<sub>61</sub>BM/DCB+DIO, as well as (e,f) their corresponding  $q_y$  and  $q_z$  scans. Gaussian fits were used to determine peak positions and FWHMs, as represented using black solid lines for the overall profiles and yellow dash lines for the individual peaks. (g) Specular XRR profiles (open symbols) and the calculated results (black solid lines) of the thin films of PTB7/PC<sub>61</sub>BM/CB (red), PTB7/PC<sub>61</sub>BM/CB+DIO (blue), PTB7/PC<sub>61</sub>BM/DCB (olive), and PTB7/PC<sub>61</sub>BM/DCB+DIO (magenta).

semiconducting polymer systems.<sup>33</sup> The improved crystallinities in the PTB7/PC<sub>61</sub>BM films are also manifested in the enhanced GIWAXS intensities (Figure 2a–d). In conjunction with GIWAXS results, we conclude that the improved crystallinity mainly stems from the increase in the number of PTB7 and PC<sub>61</sub>BM nanocrystallites, as opposed to the average size of individual nanocrystallites.

As OPV properties are linked not only to molecular stacking and crystallinity, but also to the phase-separated morphology and the relative miscibility of the components, we employed resonant soft X-ray scattering (RSOXS)<sup>17,42–44</sup> to assess spatial dimensions of phase-separated domains. Figure 3a presents RSOXS profiles of the four PTB7/PC<sub>61</sub>BM thin films as a function of the scattering vector  $q$ . The profile of PTB7/PC<sub>61</sub>BM/DCB shows one diffuse peak at  $q \sim 0.002\text{--}0.02 \text{ \AA}^{-1}$ , while those of the other three films exhibit a well-defined peak at  $q \sim 0.002\text{--}0.02 \text{ \AA}^{-1}$  and a shoulder at  $q \sim 0.01\text{--}0.05 \text{ \AA}^{-1}$ . For all four PTB7/PC<sub>61</sub>BM films, the presence of distinct yet weakly modulated scattering peaks illustrates the formation of phase-separated PTB7-rich and PC<sub>61</sub>BM-rich domains with broad size distributions. The single peak at  $q \sim 0.002\text{--}0.02 \text{ \AA}^{-1}$  in PTB7/PC<sub>61</sub>BM/DCB indicates only a one-length-scale structure at a dimension of hundreds of nanometers, whereas the double peaks at  $q \sim 0.002\text{--}0.02 \text{ \AA}^{-1}$  and  $q \sim 0.01\text{--}0.05 \text{ \AA}^{-1}$  in the other three films suggest a two-length-scale structure, in which small features correlate to a high  $q$  with a size of tens of nanometers and large features correlate to a low  $q$  with a size of hundreds of nanometers.

Inferences of RSOXS profiles were quantitatively analyzed using the pair distance distribution function,  $P(r) = [1/(2\pi^2)] \int_0^\infty I(q) q r \sin(qr) dq$ , where  $r$  is the magnitude of the distance of the autocorrelation and  $I(q)$  is the scattering intensity.<sup>17,45,46</sup> Figure 3b is the  $P(r)$

functions of four PTB7/PC<sub>61</sub>BM thin films, and their corresponding calculated  $I(q)$  are represented using black solid lines in Figure 3a. According to  $R_g^2 = 1/2 \int_0^\infty P(r) r^2 dr / \int_0^\infty P(r) dr$ ,<sup>46</sup> the radii of gyration ( $R_g$ 's) of phase-separated domains are  $176.8 \pm 0.8 \text{ nm}$  for PTB7/PC<sub>61</sub>BM/CB,  $227.7 \pm 0.3 \text{ nm}$  for PTB7/PC<sub>61</sub>BM/CB+DIO,  $216.8 \pm 0.3 \text{ nm}$  for PTB7/PC<sub>61</sub>BM/DCB, and  $236.7 \pm 0.3 \text{ nm}$  for PTB7/PC<sub>61</sub>BM/DCB+DIO, consistent with those determined from  $I(q)$  at very small angles using the Guinier equation,<sup>45</sup>  $I(q) = I(0) \exp(-q^2 R_g^2/3)$ , (in this case,  $175 \text{ nm}$  for PTB7/PC<sub>61</sub>BM/CB,  $228 \text{ nm}$  for PTB7/PC<sub>61</sub>BM/CB+DIO,  $217 \text{ nm}$  for PTB7/PC<sub>61</sub>BM/DCB, and  $237 \text{ nm}$  for PTB7/PC<sub>61</sub>BM/DCB+DIO). The similarity of  $R_g$ 's of phase separated domains obtained from different solvents substantiates that the dimensions of phase-separated PTB7-rich and PC<sub>61</sub>BM-rich domains in thin films are not strongly correlated to the solvent selection and generally occur on a similar length scale of hundreds of nanometers, considerably larger than what is typically considered for ideal BHJ morphology in OPVs. Moreover, deviations appear in the range of  $r \sim 300\text{--}1000 \text{ \AA}$  in the  $P(r)$  functions of PTB7/PC<sub>61</sub>BM/CB, PTB7/PC<sub>61</sub>BM/CB+DIO, and PTB7/PC<sub>61</sub>BM/DCB+DIO. Such kinks are indicative of the composition heterogeneity,<sup>38,39</sup> resulting from the alternation of PTB7/PC<sub>61</sub>BM nanocrystallite aggregates with amorphous PTB7 and PC<sub>61</sub>BM intermixtures in the phase-separated domains. The inhomogeneity within the phase-separated domains features a characteristic wavelength,  $L$ , of  $\sim 75 \text{ nm}$  for PTB7/PC<sub>61</sub>BM/CB,  $\sim 65 \text{ nm}$  for PTB7/PC<sub>61</sub>BM/CB+DIO, and  $\sim 45 \text{ nm}$  for PTB7/PC<sub>61</sub>BM/DCB+DIO, respectively, whereas for PTB7/PC<sub>61</sub>BM/DCB, no apparent composition heterogeneity exists within the phase-separated domains.

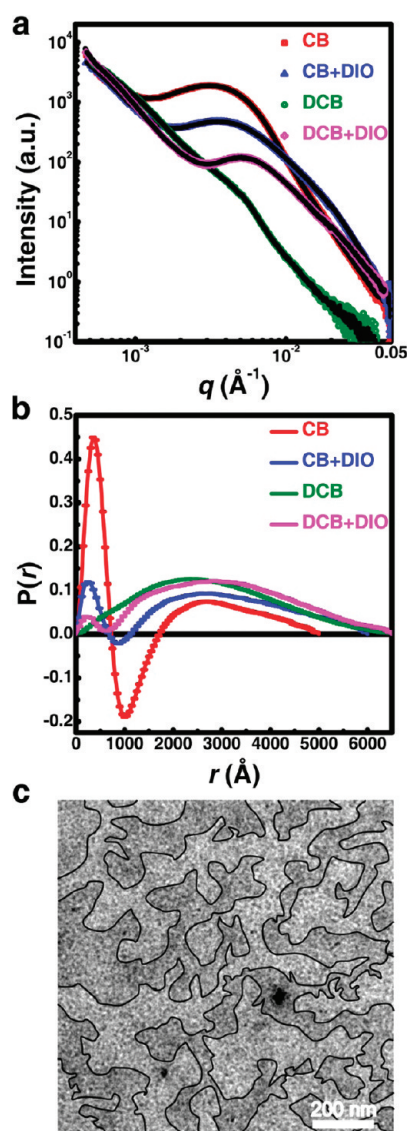


**Figure 3.** (a) RSoXS profiles (open symbols), the calculated scattering intensities  $I(q)$  (solid lines), (b) the  $P(r)$  functions of the thin films of PTB7/PC<sub>61</sub>BM/CB (red), PTB7/PC<sub>61</sub>BM/CB+DIO (blue), PTB7/PC<sub>61</sub>BM/DCB (olive), and PTB7/PC<sub>61</sub>BM/DCB+DIO (magenta), and (c) bright-field TEM image of PTB7/PC<sub>61</sub>BM/DCB+DIO thin film (black lines are added to represent the heterojunctions between PTB7-rich and PC<sub>61</sub>BM-rich domains).

To further verify the formation of hierarchical nanomorphologies, we examined the structure of a representative PTB7/PC<sub>61</sub>BM/DCB+DIO thin film using aberration-corrected transmission electron microscopy (TEM). As shown in Figure 3c, PTB7-rich and PC<sub>61</sub>BM-rich domains are differentiated by the gray scale and outlined by solid lines at heterojunctions. These domains, indeed, have a size in the range of hundreds of nanometers, which is in agreement with length scales obtained from the above analyses of the RSoXS profile and  $P(r)$  function. In addition, undulation of gray scales within each domain confirms the existence of composition heterogeneity with the dimension of tens of nanometers. Thus, the TEM data validate our picture of hierarchical nanomorphologies in PTB7/PC<sub>61</sub>BM BJH solar cells.

It should be noted that the magnitude of  $P(r)$  at constant photon energies roughly scales with the contrast factor that

directly reflects the relative miscibility of the two components.<sup>17</sup> Regarding the fact that the  $P(r)$  peak intensity of PTB7/PC<sub>61</sub>BM/CB is roughly four times higher than that of the other three films, it is evident that the PTB7/PC<sub>61</sub>BM/CB film has domains with relatively high purity ( $P(r) \sim 0.45$ ), whereas the PTB7/PC<sub>61</sub>BM films prepared using the other three solvents contain domains that are more miscible ( $P(r) \sim 0.12$ ). Inter-mixing of the PTB7 copolymer with PC<sub>61</sub>BM at a molecular level echoes recent studies on other BHJ systems.<sup>15,16,19,23</sup>

On the basis of the multiple-length-scale structural features detected by X-ray scattering techniques and electron microscopy, here we propose a refined BHJ model to elucidate the high performance of PTB7/PC<sub>61</sub>BM solar cells. As represented in Figure 4, our data demonstrate that PTB7/PC<sub>61</sub>BM blends in OPV active layers are able to develop into hierarchical nanomorphologies at three length scales ranging from several nanometers for nanocrystallites to tens of nanometers for PTB7/PC<sub>61</sub>BM nanocrystallite aggregates, and to hundreds of nanometers for PTB7/PC<sub>61</sub>BM-rich domains that are composed of nanocrystallite aggregates alternated with amorphous intermixtures of PTB7 and PC<sub>61</sub>BM molecules. We assume that these nanomorphologies have little influence on the efficiency of light absorption and exciton generation (these processes are mainly contingent on the bandgap and thickness of the absorbing material) but play a crucial role in exciton dissociation.

Exciton dissociation is a two-step process (inset of Figure 4), where an exciton is initially separated to a bound polaron pair through an ultrafast charge transfer to PC<sub>61</sub>BM, and then the bound polaron pair dissociates into free charges at heterojunctions.<sup>11,14,47–49</sup> To actively generate the bound polaron pair, the photogenerated exciton needs to meet acceptor molecules within its diffusion length that is in the range of 4–20 nm.<sup>47,50</sup> In PTB7/PC<sub>61</sub>BM solar cells, the sizes of pure PTB7 nanocrystallites are comparable to the diffusion length. Thus, it is likely that excitons photogenerated inside PTB7 nanocrystallites will diffuse to their surfaces easily. Because of the presence of PTB7 and PC<sub>61</sub>BM intermixtures between the pure PTB7 nanocrystallites, the excitons at surfaces can then readily encounter PC<sub>61</sub>BM and transfer electrons to PC<sub>61</sub>BM to form bound polaron pairs, where positive polarons situate in PTB7 copolymers and negative polarons on PC<sub>61</sub>BM. Without intermixing, the majority of excitons photogenerated within the phase-separated domains with sizes of hundreds of nanometers would not meet PC<sub>61</sub>BM prior to decay. Even though the photogenerated excitons in the amorphous regions might have a higher probability of charge transfer to PC<sub>61</sub>BM than those in the PTB7 nanocrystallite aggregates, the lower charge carrier mobilities would lead to significant geminate recombination. Crystalline structures can also reduce the charge transfer energy<sup>51</sup> and lead to a larger polaron separation distance in the charge transfer state,<sup>52</sup> thereby facilitating exciton dissociation. Therefore, it is reasonable to expect that the observed photocurrent can be attributed primarily to the dissociated excitons photogenerated in the PTB7 nanocrystallite aggregates, instead of the amorphous PTB7/PC<sub>61</sub>BM intermixed regions.

In addition, to generate photocurrent the bound polaron pairs need to migrate to the heterojunctions where they are separated into free charges. In PTB7/PC<sub>61</sub>BM solar cells, we hypothesize that the mobility of positive polarons is increased by the long segments of PTB7 copolymer chains between individual PTB7 nanocrystallites, as they can act as “highways” to transport polarons. Hence, polaron separation distances gradually increase, fostering polaron pair dissociation. In addition, the presence of the two-length-scale hierarchical heterojunctions, one being between the nanocrystallite aggregates and the amorphous regions



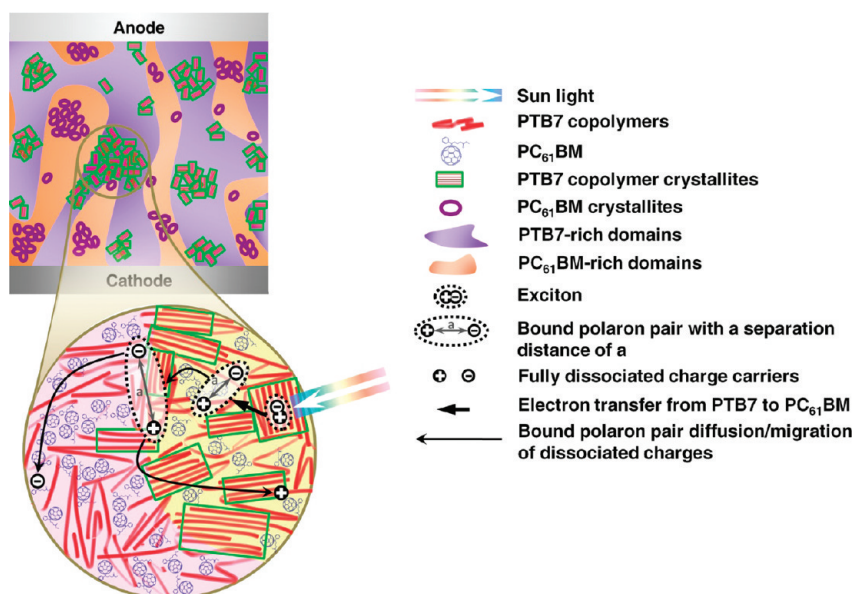


**Figure 4.** Diagrammatic hypothesis of the refined BHJ model for PTB7/fullerene solar cells.

**Table 1.** The Correlations between Morphological Features and Performance Characteristics

PTB7/PC <sub>61</sub> BM (weight ratio = 1:1)	CB	CB+DIO	DCB	DCB+DIO
crystallinity ( $\theta_c$ (°))	0.180	0.182	0.186	0.188
phase separation ( $R_g$ (nm))	$176.8 \pm 0.8$	$227.7 \pm 0.3$	$216.8 \pm 0.3$	$236.7 \pm 0.3$
heterogeneity ( $L$ (nm))	75	65		45
domain purity ( $P_{\max}(r)$ )	0.449	0.119	0.125	0.121
short-circuit current density ( $J_{SC}$ (mA/cm <sup>2</sup> ))	$10.4 \pm 0.5$	$11.1 \pm 0.5$	$9.5 \pm 0.7$	$10.9 \pm 0.4$
series resistance ( $R_S$ ( $\Omega \cdot \text{cm}^2$ ))	5.7	3.3	6.1	1.7
PCE (%)	$3.0 \pm 0.2$	$4.0 \pm 0.2$	$3.6 \pm 0.3$	$4.4 \pm 0.2$

and the other between PTB7-rich and PC<sub>61</sub>BM-rich domains, enhances polaron pair dissociation and reduces their migration distances. Consequently, the dissociated free charges eventually hop toward their respective electrodes and generate photocurrent.

Our refined BHJ model conceives correlations between structure and performance in PTB7/PC<sub>61</sub>BM solar cells that elucidate the structural impact on the short-circuit current density ( $J_{SC}$ ), the series resistance ( $R_S$ ), and the PCE. Shown in Table 1 are the correlations of morphological features versus device performance. Among the four PTB7/PC<sub>61</sub>BM thin films investigated, PTB7/PC<sub>61</sub>BM/CB has the least intermixing between PTB7 and PC<sub>61</sub>BM and the lowest crystallinity, both of which promote charge recombination, the former via increasing the required migration distance for excitons to meet PC<sub>61</sub>BM and the latter via reduction in charge mobilities that hinders the separated polarons from diffusing away, thus leading to the lowest PCE. PTB7/PC<sub>61</sub>BM/DCB exhibits the second highest crystallinity and similar intermixing between PTB7 and PC<sub>61</sub>BM to PTB7/PC<sub>61</sub>BM/CB+DIO and PTB7/PC<sub>61</sub>BM/DCB+DIO, but it does not form composition heterogeneity within the phase-separated domains, which limits the maximum number of polarons that reach a heterojunction to dissociate and contribute to the photocurrent. As a result, the smallest  $J_{SC}$  of  $9.5 \text{ mA} \cdot \text{cm}^{-2}$  and the largest  $R_S$  of  $6.8 \Omega \cdot \text{cm}^2$  were detected for this film. Although both PTB7/PC<sub>61</sub>BM/CB+DIO and PTB7/PC<sub>61</sub>BM/DCB+DIO form similar hierarchical nanomorphologies, PTB7/PC<sub>61</sub>BM/DCB+DIO develops a smaller characteristic wavelength of composition heterogeneity and higher

crystallinity, which favor exciton dissociation and free charge transport, and thus this device exhibits the lowest  $R_S$  ( $1.7 \Omega \cdot \text{cm}^2$ ) and the highest PCE (4.4%).

To further demonstrate that hierarchical nanomorphologies with optimum crystallinity and miscibility promote exciton dissociation and thus improve device performance, we quantitatively analyzed the photocurrent against the effective applied bias voltage. As shown in Figure 5, the photocurrent in all four films ( $J_{ph} = J - J_D$ ) linearly increases with voltage at low effective field ( $V_0 - V \leq 0.1$ ) and gradually saturates, independent of  $V$ , at high effective field ( $V_0 - V > 0.1$ ). Following Mihailetschi et al.<sup>14,47,48,52–54</sup> (see Supporting Information), the generation rates of free charges at the open-circuit voltage were estimated to be  $3.9 \times 10^{27} \text{ m}^{-3} \text{ s}^{-1}$  for PTB7/PC<sub>61</sub>BM/CB,  $5.0 \times 10^{27} \text{ m}^{-3} \text{ s}^{-1}$  for PTB7/PC<sub>61</sub>BM/DCB,  $6.2 \times 10^{27} \text{ m}^{-3} \text{ s}^{-1}$  for PTB7/PC<sub>61</sub>BM/CB+DIO, and  $7.5 \times 10^{27} \text{ m}^{-3} \text{ s}^{-1}$  for PTB7/PC<sub>61</sub>BM/DCB+DIO, which correlate well to both the corresponding nanomorphology and the PCEs.

In summary, we investigated performance-related structures in PTB7/PC<sub>61</sub>BM solar cells at different length scales using multiple scattering techniques. Contrary to the commonly accepted picture of ideal BHJ morphology, we demonstrated that the superior performance of PTB7/PC<sub>61</sub>BM solar cells correlates to hierarchical morphologies with optimum crystallinity and intermixing of PTB7 with PC<sub>61</sub>BM. Our refined BHJ model elaborates two advantages of these hierarchical nanomorphologies: (1) several nanometers of PTB7 nanocrystallites surrounded by PTB7 and PC<sub>61</sub>BM

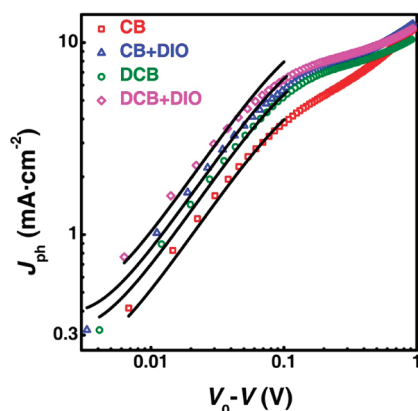


**Figure 5.** Effective photocurrent density ( $J_{ph} = J - J_D$ ) as a function of the effective applied voltage ( $V_0 - V$ ) of PTB7/PC<sub>61</sub>BM OPV devices fabricated using CB (red), CB+DIO (blue), DCB (olive), and DCB+DIO (magenta) as solvents.

intermixtures are beneficial to gain a high yield of electron transfer to form bound polaron pairs; and (2) tens of nanometers of PTB7 nanocrystallite aggregates and amorphous PTB7 and PC<sub>61</sub>BM intermixed regions within hundreds of nanometers of extended PTB7-rich domains are optimum for polarons to escape Coulombic capture and thus to achieve polaron pair dissociation at the heterojunctions. Consequently, exciton dissociation in such hierarchical nanomorphologies can be significantly enhanced, leading to the superior performance of PTB7/fullerene solar cells. Given that analogous multiple-length-scale nanostructures have also been observed in the related PTB/PC<sub>61</sub>BM copolymer blends (Supporting Information Figure S5), we believe these hierarchical nanomorphologies represent a structural generality in the PTB copolymer series when blended with fullerenes in OPV devices. Our model helps identify key structural features of PTB7/PC<sub>61</sub>BM necessary for optimal device performance. New insights of performance-related structures afforded by the current study should aid in the rational design of even higher performance polymeric solar cells.

## ■ ASSOCIATED CONTENT

**Supporting Information.** Experimental procedures of GIWAXS, XRR, RSoXS, SANS, and device fabrication; SANS data of the PTB7 copolymer in deuterated chlorobenzene; discussions on the instrumental resolutions of GIWAXS and XRR; RSoXS profiles and the corresponding  $P(r)$  functions of PTB series of copolymers blended with PC<sub>61</sub>BM; bright-field TEM image and high-resolution SEM image of PTB7/PC<sub>61</sub>BM/DCB+DIO thin film,  $J$ – $V$  characteristics and physical parameters of PTB7/PC<sub>61</sub>BM OPV devices, and estimation of free charge generation rates. This material is available free of charge via the Internet at <http://pubs.acs.org>.

## ■ AUTHOR INFORMATION

### Corresponding Author

\*E-mail: (W.C.) [wchen@anl.gov](mailto:wchen@anl.gov); (S.B.D.) [darling@anl.gov](mailto:darling@anl.gov); (L.Y.) [lupingyu@uchicago.edu](mailto:lupingyu@uchicago.edu).

## ■ ACKNOWLEDGMENT

W.C. gratefully acknowledges financial support from Argonne Director's Postdoctoral Fellowship. L.Y., T.X. and F.H. acknowledge

support from NSF, NSF-MRSEC, AFOSR, and DOE on the synthesis of polymers. This work was partially supported by a University of Chicago-Argonne Strategic Collaborative Initiative Seed Grant. We thank Dr. Zhang Jiang for helpful discussions and sharing XRR of the thick polymer film. Use of the Advanced Photon Source (APS), the Electron Microscopy Center (EMC) for Materials Research, and the Center for Nanoscale Materials (CNM) at Argonne National Laboratory was supported by the U.S. Department of Energy, Office of Science, Office of Basic Energy Sciences, under Contract No. DE-AC02-06CH11357. The ALS at Lawrence Berkeley National Laboratory is supported by the Director, Office of Science, Office of Basic Energy Sciences, of the U.S. Department of Energy under Contract No. DE-AC02-05CH11231. A portion of this research was conducted at the Center for Nanophase Materials Sciences, which is sponsored at Oak Ridge National Laboratory by the Office of Basic Energy Sciences, U.S. Department of Energy. The submitted manuscript has been created by UChicago Argonne, LLC, Operator of Argonne National Laboratory ("Argonne"). Argonne, a U.S. Department of Energy Office of Science laboratory, is operated under Contract No. DE-AC02-06CH11357. Certain commercial equipment, instruments, or materials are identified in this paper to foster understanding. Such identification does not imply recommendation or endorsement by the National Institute of Standards and Technology, nor does it imply that the materials or equipment identified are necessarily the best available for the purpose.

## ■ REFERENCES

- (1) Shrotriya, V. *Nat. Photonics* **2009**, 3, 447–449.
- (2) Yu, G.; Gao, J.; Hummelen, J. C.; Wudl, F.; Heeger, A. J. *Science* **1995**, 270, 1789–1791.
- (3) Halls, J. J. M.; Walsh, C. A.; Greenham, N. C.; Marseglia, E. A.; Friend, R. H.; Moratti, S. C.; Holmes, A. B. *Nature* **1995**, 376, 498–500.
- (4) Liang, Y.; Yu, L. *Acc. Chem. Res.* **2010**, 43, 1227–1236.
- (5) Liang, Y.; Xu, Z.; Xia, J.; Tsai, S. T.; Wu, Y.; Li, G.; Ray, C.; Yu, L. *Adv. Mater.* **2010**, 22, E135–E138.
- (6) Son, H. J.; Wang, W.; Xu, T.; Liang, Y.; Wu, Y.; Li, G.; Yu, L. *J. Am. Chem. Soc.* **2011**, 133, 1885–1894.
- (7) Chen, H.-Y.; Hou, J.; Zhang, S.; Liang, Y.; Yang, G.; Yang, Y.; Yu, L.; Wu, Y.; Li, G. *Nat. Photonics* **2009**, 3, 649–653.
- (8) Price, S. C.; Stuart, A. C.; Yang, L.; Zhou, H.; You, W. *J. Am. Chem. Soc.* **2011**, 133, 4625–4631.
- (9) Chu, T.-Y.; Lu, J.; Beaupré, S.; Zhang, Y.; Pouliot, J.-R.; Wakim, S.; Zhou, J.; Leclerc, M.; Li, Z.; Ding, J.; Tao, Y. *J. Am. Chem. Soc.* **2011**, 133, 4250–4253.
- (10) Slot, J. E.; He, X.; Huck, W. T. S. *Nano Today* **2010**, 5, 231–242.
- (11) Deibel, C.; Strobel, T.; Dyakonov, V. *Adv. Mater.* **2010**, 22, 4097–4111.
- (12) Thompson, B. C.; Fréchet, J. M. J. *Angew. Chem., Int. Ed.* **2008**, 47, 58–77.
- (13) Günes, S.; Neugebauer, H.; Sariciftci, N. S. *Chem. Rev.* **2007**, 107, 1324–1338.
- (14) Carsten, D.; Vladimir, D. *Rep. Prog. Phys.* **2010**, 73, 096401.
- (15) McNeill, C. R.; Watts, B.; Thomsen, L.; Belcher, W. J.; Greenham, N. C.; Dastoor, P. C. *Nano Lett.* **2006**, 6, 1202–1206.
- (16) Collins, B. A.; Gann, E.; Guignard, L.; He, X.; McNeill, C. R.; Ade, H. *J. Phys. Chem. Lett.* **2010**, 1, 3160–3166.
- (17) Swaraj, S.; Wang, C.; Yan, H.; Watts, B.; Lüning, J.; McNeill, C. R.; Ade, H. *Nano Lett.* **2010**, 10, 2863–2869.
- (18) Treat, N. D.; Brady, M. A.; Smith, G.; Toney, M. F.; Kramer, E. J.; Hawker, C. J.; Chabinyc, M. L. *Adv. Energy Mater.* **2011**, 1, 82–89.
- (19) Chen, D.; Liu, F.; Wang, C.; Nakahara, A.; Russell, T. P. *Nano Lett.* **2011**, 11, 2071–2078.
- (20) Parnell, A. J.; Dunbar, A. D. F.; Pearson, A. J.; Staniec, P. A.; Dennison, A. J. C.; Hamamatsu, H.; Skoda, M. W. A.; Lidzey, D. G.; Jones, R. A. L. *Adv. Mater.* **2010**, 22, 2444–2447.

- (21) Kiel, J. W.; Kirby, B. J.; Majkrzak, C. F.; Maranville, B. B.; Mackay, M. E. *Soft Matter* **2010**, *6*, 641.
- (22) Yan, H.; Swaraj, S.; Wang, C.; Hwang, I.; Greenham, N. C.; Groves, C.; Ade, H.; McNeill, C. R. *Adv. Func. Mater.* **2010**, *20*, 4329–4337.
- (23) Chen, D.; Nakahara, A.; Wei, D.; Nordlund, D.; Russell, T. P. *Nano Lett.* **2011**, *11*, 561–567.
- (24) Cates, N. C.; Gysel, R.; Beiley, Z.; Miller, C. E.; Toney, M. F.; Heeney, M.; McCulloch, I.; McGehee, M. D. *Nano Lett.* **2009**, *9*, 4153–4157.
- (25) Cates, N. C.; Gysel, R.; Dahl, J. E. P.; Sellinger, A.; McGehee, M. D. *Chem. Mater.* **2010**, *22*, 3543–3548.
- (26) Guo, J.; Ohkita, H.; Benten, H.; Ito, S. *J. Am. Chem. Soc.* **2010**, *132*, 6154–6164.
- (27) Scharber, M. C.; Mühlbacher, D.; Koppe, M.; Denk, P.; Waldauf, C.; Heeger, A. J.; Brabec, C. J. *Adv. Mater.* **2006**, *18*, 789–794.
- (28) Peet, J.; Kim, J. Y.; Coates, N. E.; Ma, W. L.; Moses, D.; Heeger, A. J.; Bazan, G. C. *Nat. Mater.* **2007**, *6*, 497–500.
- (29) Moulé, A. J.; Meerholz, K. *Adv. Mater.* **2008**, *20*, 240–245.
- (30) Yao, Y.; Hou, J.; Xu, Z.; Li, G.; Yang, Y. *Adv. Func. Mater.* **2008**, *18*, 1783–1789.
- (31) Lee, J. K.; Ma, W. L.; Brabec, C. J.; Yuen, J.; Moon, J. S.; Kim, J. Y.; Lee, K.; Bazan, G. C.; Heeger, A. J. *J. Am. Chem. Soc.* **2008**, *130*, 3619–3623.
- (32) Moon, J. S.; Takacs, C. J.; Cho, S.; Coffin, R. C.; Kim, H.; Bazan, G. C.; Heeger, A. J. *Nano Lett.* **2010**, *10*, 4005–4008.
- (33) Rogers, J. T.; Schmidt, K.; Toney, M. F.; Kramer, E. J.; Bazan, G. C. *Adv. Mater.* **2011** ASAP.
- (34) Hoven, C. V.; Dang, X.-D.; Coffin, R. C.; Peet, J.; Nguyen, T.-Q.; Bazan, G. C. *Adv. Mater.* **2010**, *22*, E63–E66.
- (35) Szarko, J. M.; Guo, J.; Liang, Y.; Lee, B.; Rolczynski, B. S.; Strzalka, J.; Xu, T.; Loser, S.; Marks, T. J.; Yu, L.; Chen, L. X. *Adv. Mater.* **2010**, *22*, 5468–5472.
- (36) Guo, J.; Liang, Y.; Szarko, J.; Lee, B.; Son, H. J.; Rolczynski, B. S.; Yu, L.; Chen, L. X. *J. Phys. Chem. B* **2010**, *114*, 742–748.
- (37) Verploegen, E.; Mondal, R.; Bettinger, C. J.; Sok, S.; Toney, M. F.; Bao, Z. *Adv. Func. Mater.* **2010**, *20*, 3519–3529.
- (38) Bennington, S. M.; et al. *J. Phys.: Condens. Matter* **2000**, *12*, L451.
- (39) Smilgies, D.-M. *J. Appl. Crystallogr.* **2009**, *42*, 1030–1034.
- (40) Sentenac, D.; Shalaginov, A. N.; Fera, A.; de Jeu, W. H. *J. Appl. Crystallogr.* **2000**, *33*, 130–136.
- (41) Russell, T. P. *Mater. Sci. Rep.* **1990**, *5*, 171–271.
- (42) Swaraj, S.; Wang, C.; Araki, T.; Mitchell, G.; Liu, L.; Gaynor, S.; Deshmukh, B.; Yan, H.; McNeill, C. R.; Ade, H. *Eur. Phys. J. Spec. Top.* **2009**, *167*, 121–126.
- (43) Wang, C.; Hexemer, A.; Nasiatka, J.; Chan, E. R.; Young, A. T.; Padmore, H. A.; Schlotter, W. F.; Lüning, J.; Swaraj, S.; Watts, B.; Gann, E.; Yan, H.; Ade, H. *IOP Conf. Ser.: Mater. Sci. Eng.* **2010**, *14*, 012016.
- (44) Virgili, J. M.; Tao, Y.; Kortright, J. B.; Balsara, N. P.; Segalman, R. A. *Macromolecules* **2007**, *40*, 2092–2099.
- (45) Glatter, O.; Kratky, O. *Small Angle X-ray Scattering*; Academic Press: London, 1982.
- (46) Feigin, L. A.; Svergun, D. I. *Structure Analysis by Small-Angle X-Ray and Neutron Scattering*; Plenum Press: New York, 1987; p 335.
- (47) Deibel, C.; Dyakonov, V.; Brabec, C. J. *IEEE J. Sel. Top. Quantum Electron* **2010**, *16*, 1517–1527.
- (48) Clarke, T. M.; Durrant, J. R. *Chem. Rev.* **2010**, *110*, 6736–6767.
- (49) Blom, P. W. M.; Mihailetchi, V. D.; Koster, L. J. A.; Markov, D. E. *Adv. Mater.* **2007**, *19*, 1551–1566.
- (50) Shaw, P. E.; Ruseckas, A.; Samuel, I. D. W. *Adv. Mater.* **2008**, *20*, 3516–3520.
- (51) Vandewal, K.; Oosterbaan, W. D.; Bertho, S.; Vriendts, V.; Gadisa, A.; Lutsen, L.; Vanderzande, D.; Manca, J. V. *Appl. Phys. Lett.* **2009**, *95*, 123303–3.
- (52) Strobel, T.; Deibel, C.; Dyakonov, V. *Phys. Rev. Lett.* **2010**, *105*, 266602.
- (53) Mihailetchi, V. D.; Koster, L. J. A.; Hummelen, J. C.; Blom, P. W. M. *Phys. Rev. Lett.* **2004**, *93*, 216601.
- (54) Limpinsel, M.; Wagenpfahl, A.; Mingeback, M.; Deibel, C.; Dyakonov, V. *Phys. Rev. B* **2010**, *81*, 085203.